PAN

Opto-Electronics Review

journal homepage: https://journals.pan.pl/opelre

Sensor performance and cut-off wavelength tradeoffs of III-V focal plane arrays

Jonathan Ch. James*, Terence L. Haran, Sarah E. Lane

Electro-Optical Systems Laboratory, Georgia Tech Research Institute, 925 Dalney St. NW, Atlanta, GA 30332, USA

Article info

Article history:
Received 04 Nov. 2022
Received in revised form 04 Jan. 2023
Accepted 17 Jan. 2023
Available on-line 24 Feb. 2023

Keywords:
Infrared focal plane arrays; III-V semiconductor infrared detector technologies; infrared sensor performance modelling; infrared sensor design; mid-wave and long-wave infrared sensors.

Abstract

Infrared detector technologies engineered from III-V semiconductors such as strained-layer superlattice, quantum well infrared photodetectors, and quantum dot infrared photodetectors provide additional flexibility to engineer bandgap or spectral response cut-offs compared to the historical high-performance detector technology of mercury/cadmium/telluride. The choice of detector cut-off depends upon the sensing application for which the system engineer is attempting to maximize performance within an expected ensemble of operational scenarios that define objects or targets to be detected against specific environmental backgrounds and atmospheric conditions. Sensor performance is typically characterised via one or more metrics that can be modelled or measured experimentally. In this paper, the authors will explore the impact of detector cut-off wavelength with respect to different performance metrics such as noise equivalent temperature difference and expected target detection or identification ranges using analytical models developed for several representative sensing applications encompassing a variety of terrestrial atmospheric conditions in the mid-wave and long-wave infrared wavelength bands. The authors will also report on their review of recently published literature concerning the relationships between cut-off wavelength and the other detector performance characteristics such as quantum efficiency or dark current for a variety of detector technologies.

1. Introduction

High performance infrared detector focal plane arrays (FPA) have historically utilized the ternary semiconductor compound mercury/cadmium/telluride (HgCdTe) for operation in the 3–5 μm mid-wave infrared (MWIR) and 8–12 μm long-wave infrared (LWIR) wavebands. While HgCdTe offers several significant advantages, including high quantum efficiency (QE), that make it the preferred material for demanding applications, there are several drawbacks associated with HgCdTe devices. Uniformity is one challenge for HgCdTe devices, particularly for LWIR devices, due to composition variations across a detector FPA that occur during the fabrication process (leading to variability in cut-off wavelength), as well as to 1/f noise, which causes uniformity to vary over time and therefore be more difficult to correct via image processing [1].

The drawbacks associated with HgCdTe have led to continued interest in detectors comprised of III-V materials, including type II strained-layer superlattices (T2SLSs), quantum well infrared photodetectors (QWIP), and bulk barrier detectors such as nBn devices, since they could potentially leverage the extensive industrial base that exists for those materials to ultimately provide larger format FPAs at lower cost [2]. These advantages have been offset to date by lower performance in terms of QE and dark current when compared to HgCdTe or other benchmark materials [3].

In previous papers [4, 5], the authors presented the results of analyses to evaluate system-level performance (quantified by the range at which a human observer can detect or identify a relevant target) to determine appropriate goals for detector design parameters such as QE, dark current density, quantum well capacity, downstream readout noise, well fill, image frame rate, frame averaging, and residual fixed pattern noise (RFPN). Although optimum

*Corresponding author at: chris.james@gtri.gatech.edu

https://doi.org/10.24425/opelre.2023.144570
1896-3757/ Association of Polish Electrical Engineers (SEP) and Polish Academic of Sciences (PAS). Published by PAS

design goals for these parameters are application specific, the authors were able to make several general observations based on the results of the analyses. A primary observation is that, for relatively low levels of dark current (over several orders of magnitude), there is effectively no change in range performance for a particular QE even across a variety of environmental conditions and system-level optical characteristics. In these cases, design trades to improve QE will offer the most benefit to system performance. For LWIR applications with typically high flux scenes, another option would be to pair low dark current FPAs with digital read-out and integration circuits offering larger effective well capacities to improve performance even for low QE. However, for relatively high levels of dark current (as reported for some III-V devices), system performance will degrade regardless of QE, and therefore reducing dark current should be the priority [4].

Another significant observation was that an FPA with poorly corrected uniformity or high RFPN can lead to system performance equivalent to an FPA with good uniformity or low RFPN but relatively low QE or dark current that is two (or more) orders worse in magnitude. Furthermore, it was found that low RFPN is the primary detector characteristic for determining system performance assuming a finite well size. Therefore, prioritization of uniformity improvements may offer an FPA manufacturer an easier path to increase system performance [5].

One aspect of the previous sensor design trade space analyses that was not explored in depth was the impact of detector spectral response bandwidth on detector- and system-level performance. While the previous analyses did look for performance trends in the MWIR and LWIR bands, separately, they made simple assumptions of fixed response bands of 3.5–5.0 μm (with a CO_2 notch filter) for the MWIR and 8.0–10.0 μm in the LWIR. Detector QE and dark current performance are tied to the cut-off wavelengths and the strength of those ties are dependent on the detector material technology. With $Hg_{1-x}Cd_xTe$ detectors, cut-offs are controlled by alloy composition factor x, which leads to relatively simple relationships defining the spectral response of those detectors. With III-V detectors, the spectral response is more dependent on absorber thickness rather than alloy composition and the flexibility of the meta-structure design can lead to more complex relationships defining the spectral responses. Therefore, the objective of the analysis conducted for this paper was to explore this remaining aspect of the sensor design trade space.

Section 2 of this paper will review the sensor design performance drivers and metrics used for the analysis. Section 3 will provide an updated comparison of published experimental detector and FPA performance for the various detector technologies under consideration with the addition of new data reported in the period between the publication of the previous paper and this paper. Section 4 will review the computational tools and constraints used during the analysis, and section 5 will present the results of the analysis. Section 6 will conclude the paper with general observations that the authors made from the results.

2. Infrared system performance drivers and metrics

Conceptually, a cooled infrared sensor system design can be broken down into three-four major subsystems: the optical lens system that forms infrared images, and which may include mechanical image scanning or stabilisation of the sensor line of sight, the FPA of detector elements in the image plane of the optical system, the silicon semiconductor read-out integrated circuit (ROIC) that is hybridised to the FPA, and the cryo-cooler dewar assembly in which the hybridised FPA resides and which also may feature optical elements. As depicted in Fig. 1, each of these subsystems have design parameters that define overall system performance as assessed via metrics such as: the noise equivalent temperature difference (NETD), which is the differential target temperature required to achieve unity signal to noise ratio (SNR) at the detector, the minimum resolvable temperature difference (MRTD), which is the spatial frequency dependent differential target temperature at which an observer can no longer discern that difference, the ground resolved distance (GRD), which characterises the spatial resolution in terms of the pixel area projected on the ground, or the edge response, which quantifies image sharpness as measured along a high contrast edge feature. These metrics are frequently used when comparing the performance of infrared sensor systems as they can be characterised in a laboratory setting with relative ease. However, these metrics may not have a directly understandable relationship to metrics that end-users of a system deem important.

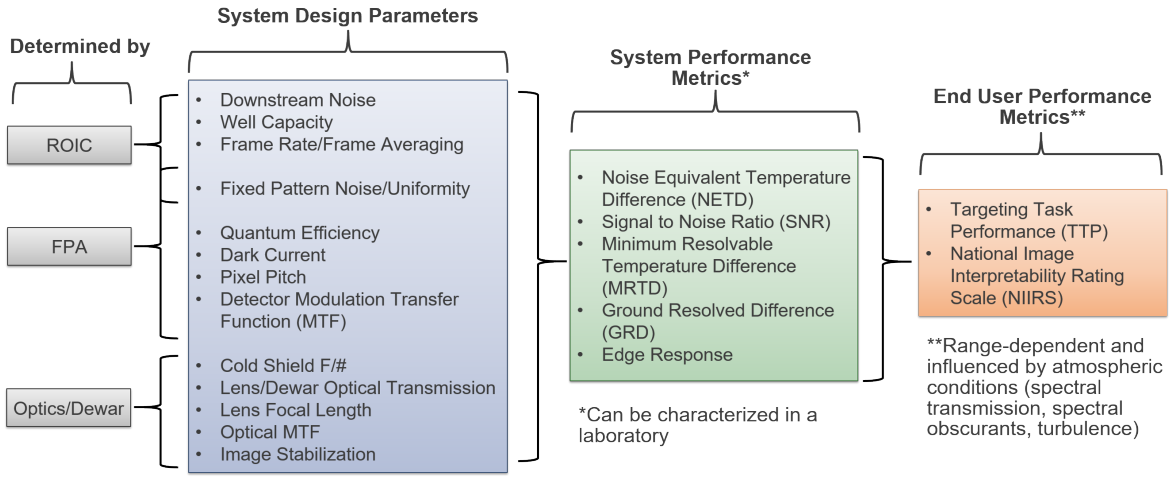

Fig. 1. Key infrared system performance drivers and metrics.

Metrics such as targeting task performance (TTP) [6], where the probability that a human observer using the system can successfully perform a target detection or classification task is assessed, may be more relevant. End-user metrics typically depend upon all aspects of system performance, such as sensitivity and perceived image resolution, in the expected operational environment and are more difficult to characterise as they are dependent on target range and may require the collection of statistical performance data from multiple observers.

The dependency of end-user metrics upon target range is partly due to the influence of the atmospheric conditions prevailing between the sensor and the target in ways that the laboratory-characterised system performance metrics are not. For example, the spectral transmission of the atmosphere is plotted in Fig. 2 for several target ranges as calculated using the MODTRAN radiative transfer atmospheric modelling software tool assuming the Mid-Latitude Summer atmosphere model and a horizontal sea-level path with an aerosol distribution producing 23 km of visibility. As can be seen in the transmission plots, both of 3–5 μm MWIR and 8–14 μm LWIR atmospheric transmission windows are characterised by a wavelength-dependent extinction that is stronger at the edges of the windows as the target range (path length) increases causing the shape of the window to erode.

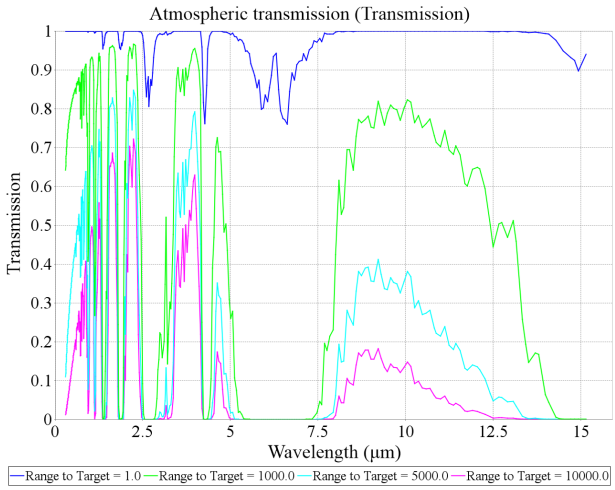

Fig. 2. Spectral transmission for MODTRAN Mid-Latitude Summer atmosphere with a 23 km visibility as a function of target range.

The spectral extinction characteristics within these windows are a result of the contributions of the multiple types of gas molecules and aerosols, but the bulk of the extinction is due to continuum absorption by water vapour (H_2O), especially for the LWIR window, and, also by carbon dioxide (CO_2) for the MWIR window. The average CO_2 concentration is relative consistent across the globe and is typically treated as a function of altitude, but H_2O concentration is highly variable [7]. Therefore, H_2O concentration along with atmospheric temperature and pressure can serve as variables for exploring the impact of varying spectral extinction profiles to end-user system performance across multiple weather environments.

The impact of atmospheric extinction on end-user performance is twofold: loss of emitted and/or reflected energy from the objects in the scene the user is trying to observe but also a scattering of energy that is manifested as an increase in observed background energy and hence noise. The spectral distribution of this extinction, for ranges of interest to the end-user, when combined with the spectral distribution of the scene radiance and the spectral response of the sensor will lead to a spectral dependence of the end-user performance metrics that can be very different than that for the system-level performance metrics that are characterised with measurement apparatuses involving very short atmospheric path lengths. Therefore, system design trade space analyses trying to determine optimum detector cut-off wavelengths using system-level performance metrics may lead to different conclusions than those analyses using end-user performance metrics. The analyses described in this paper were performed to explore the potential discrepancies that may occur in the results using one metric type or the other.

3. Recently reported infrared detector performance

Prior to starting the design trade space analyses, the authors revisited and updated their survey of recent performance being reported by developers of both HgCdTe and III-V detector material systems. The purpose of this survey was to determine the current state of the art values for QE, dark current, and RFPN reported for FPAs fabricated from these material systems and covered reports published over approximately a nine-year period between 2013 and 2022. The survey includes 68 unique references from a variety of different institutions and organizations [8–75] and includes FPAs with variations in substrate removal, anti-reflection coatings, and operating temperature. The T2SLS values reported here only include results published since the authors' last survey [5], and the QE and dark current charts focus on results from test arrays and production FPAs rather than single photodiodes, which were included in the previous publications.

Figure 3 illustrates reported QEs as a function of device cut-off wavelength for the material systems specified by data point colour/shape. HgCdTe QE values varied from 60–80% in the MWIR, similar to the authors' previous surveys [4, 5]. However, HgCdTe QE values included in this survey include bi-spectral MWIR/MWIR detectors from Ref. 13. HgCdTe QE values in the LWIR include values lower than the 50–80% previously reported, which represent measured QEs during optimization of 640×512, 15 μm pitch FPAs [8]. Overall, the HgCdTe performance is still consistent with commercial products and previously reported values [77]. T2SLS QE values ranged from 25–80% in MWIR and 15–50% in LWIR, consistent with the authors' previous surveys. Limited data points were found for bulk XBn devices, but that material appears to have QE consistent with T2SLS in the MWIR. Reported QE for QWIP devices in the LWIR ranged from 25–60%. These QWIP devices have lower QE due to their inability to absorb normally incident photons, and generally exhibit low photoelectric gain, which leads to conversion efficiencies approximately 10% or less, significantly below other material systems that offer near-unity gain [77]. The results do show an overall improvement in QWIP QE since the previous survey from 2019 [5], where the maximum observed QE was less than 30%. However, this survey adds references from 2015 [26] and 2018 [12] that were not included previously.

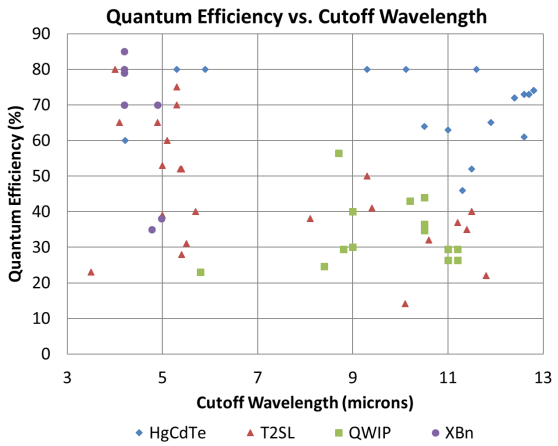

Fig. 3. Reported quantum efficiency performance achieved for various detector material technologies as a function of cut-off wavelength.

Reported dark current values are shown in Fig. 4 as a function of the inverse cut-off wavelength/operating temperature product. For reference, the "Rule 07" heuristic for the HgCdTe dark current is shown along with lines representing dark currents ten and one hundred times worse than Rule 07 [76]. The reported dark currents show consistent trends to previously reported data but represent an overall improvement compared to a previous review published in 2011 [78] and the authors' previous publications [4, 5]. As expected, the dark current for HgCdTe is generally below the Rule 07 heuristic; those below are found in Refs. 45–50. The authors' previous surveys showed that T2SLS devices had wide variability in dark current, and in most cases were 10–100 (or more) times worse than Rule 07, although there were several cases where T2SLS dark current was within one order of magnitude of Rule 07. This survey shows a vast improvement in T2SLS devices in both the MWIR and LWIR, where dark currents are approaching those of HgCdTe devices. Dark currents for bulk XBn devices show a similar improvement to T2SLS devices since the authors' last survey, with dark currents approaching ten times Rule 07. There is limited data available for QWIP devices, and although the dark currents near ten times Rule 07 indicate some improvement since the authors' last survey, most dark currents are still almost more than two orders of magnitude worse than Rule 07, which exacerbates the challenges posed by their low conversion efficiencies.

These results indicate that state-of-the-art T2SLS devices have QEs that are roughly equivalent to HgCdTe in the MWIR and 30% (or more) below HgCdTe in the LWIR with corresponding dark currents that are equivalent to HgCdTe in the MWIR and approaching HgCdTe in the LWIR, with several instances at Rule 07, (Rule 07 is normalised for cut-off and operating temperature), an improvement over values reported previously [5]. Current QWIP devices have QEs that are roughly equivalent to recently reported lower HgCdTe QEs in LWIR with corresponding dark currents that are 10–100 times higher than HgCdTe and Rule 07. Only one additional XBn publication was identified in this survey, but the limited data points indicate QE within the range of T2SLS devices. The XBn MWIR dark currents are higher than previously reported (due to a plotting error) and are on the order of T2SLS arrays.

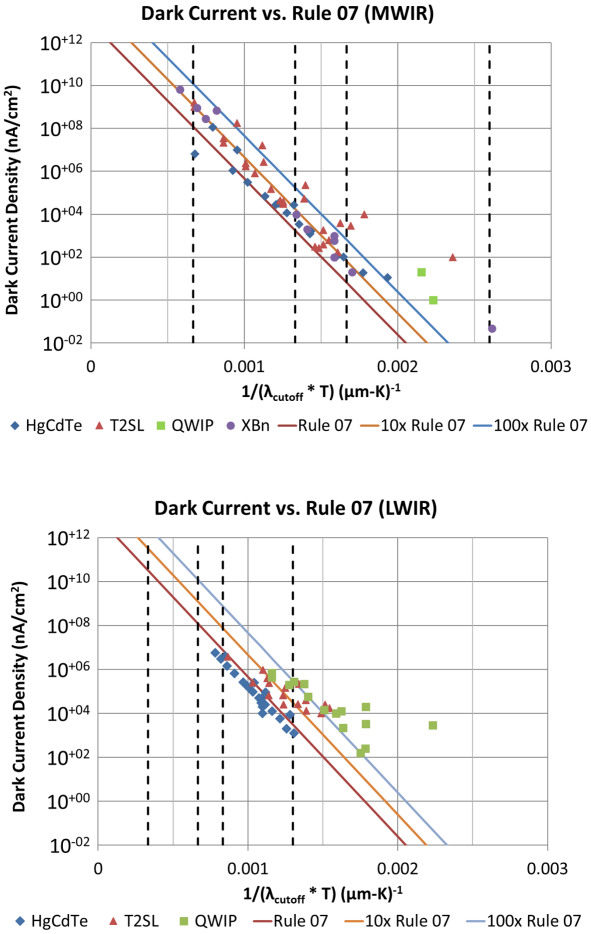

Fig. 4. Recently reported dark current measurements for various detector materials with MWIR (top) and LWIR (bottom) wavelength cut-offs. The vertical lines, left to right, represent detectors at 300, 150, 120, and 77 K with a 5 µm cut-off (MWIR, top) and a 10 µm cut-off (LWIR, bottom).

RFPN is a standard measure of uniformity and is often reported in the literature using several different metrics, including as a ratio of standard deviation to mean signal for a uniform scene or as a percentage of total dynamic range, but the ratio of RFPN to NETD as a function of well fill percentage is preferred for modelling purposes due to the ease of incorporating it into photon-counting modelling tools such as night vision integrated performance model (NV-IPM). Since non-uniformity changes over time, as well as between device cooldowns, rigorous RFPN reporting will provide these data for several time samples relative to the most recent non-uniformity correction (NUC) and for repeated cooldown cycles without performing a fresh NUC. These data provide a measure of device stability *vs*. time and cooldown cycles, which is important to minimize need for frequent NUCs that may be operationally undesirable. While there are limited published data that meet these requirements, recent reports describing RFPN were located for each material system considered in this analysis. These data indicate that III-V devices show excellent uniformity for both MWIR and LWIR bands *vs*. time and over multiple cooldown cycles, with typical RFPN values below 50% of NETD with little change over time. HgCdTe uniformity varies widely by device but tends to be less stable than T2SLS over time and multiple cooldown cycles, with typical RFPN values above 70% of

NETD. This study only addressed RFPN and did not consider operability or cluster defects, improvements in which may favour III-V materials [17, 21, 23, 61, 62, 68–75].

4. Performance analysis overview

As with the authors' previous papers [4, 5], the analysis described here was performed using the NV-IPM developed by the U.S. Army Night Vision and Electronic Sensors Directorate (NVESD). In order to assess the relative importance of detector cut-off wavelengths with respect to both system-level and end-user performance, a series of simulations were performed to iterate the relevant design parameters for a hypothetical infrared imaging system over the range of values seen in current state of the art technology in order to analyse the predicted range performance associated with each combination of values. Using the unique capabilities of NV-IPM to loop efficiently over a variety of inputs, a matrix of parameters was developed for each component of the system as shown in Fig. 5. This analysis assumed a hypothetical imager designed for tactical applications involving targeting or surveillance tasks performed by a human observer. Both MWIR and LWIR variants of the design were considered in the, analysis. For consistency with the authors' previous analyses these parameters are unchanged save for a down selection of the values for certain parameters to reduce the size of the analysis trade space. The reader is referred to Fig. 1 in both of the previous publications for the test matrices that correspond to Fig. 5 here. While the study was intended to present an advanced, modern, infrared imaging system using design values supported by published literature, the FPA was modelled based on assumed values and did not represent a specific FPA part from any particular source.

As with the previous analyses, the spectral responses of the detectors in modelled FPA designs were assumed to be flat top-hat shapes, but for this analysis both the response cut-on and cut-off wavelengths were varied. For the MWIR FPAs, the cut-on wavelengths ranged 2.8 to 3.2 µm, and the cut-off wavelengths ranged from 4.1 to 5.4 µm. For the LWIR FPAs, the cut-on wavelengths ranged 7.0 to 8.4 µm, and the cut-off wavelengths ranged from 8.2 to 14.0 µm. Three values of effective in-band QE were assumed: 30, 50, and 70%. Detector dark current values were selected based on the performance "knees" that were observed in the previously reported trade studies with 2 µA/cm^2 being used for the MWIR sensor model and 200 µA/cm^2 for the LWIR model. The RFPN of the FPA was modelled by assuming 3D noise values for σ_V (row pattern noise), σ_H (column pattern noise), and σ_{VH} (random pattern noise) of 0, 0, and $0.1 \cdot \sigma_{TVH}$ (non-fixed spatio-temporal noise). Hypothetical ROIC values for well size (10 million electrons), downstream noise, read time, and frame rate were modelled based on commercially available analogue ROICs with 15-micron pixel pitch.

The optical lens systems modelled in the analysis were identical to the two F/2.0 and F/4.0 optical designs that were modelled in the previous analyses. As in the previous analyses, the temperature of the optics was modelled as having an elevated temperature relative to the surrounding environment, as linked to the temperature of the atmospheric conditions being modelled, to incorporate any performance impact associated with the changes in the spectral dependence of the optics self-emissions relative to environment.

The performance metrics calculated for the design trade space included the system NETD as measured in the laboratory (at-aperture), the TTP metric target detection (F/2.0 optic) or identification (F/4.0) ranges, and the system NETDs corresponding to those ranges. The targeting task used for this analysis assumed a standard vehicle target as defined in the NV-IPM manual with corresponding task difficulty V50 values for detection and identification.

In the previously reported analyses, up to four different atmospheric conditions were modelled to reflect a range of real-world environments. For the analysis reported in this paper, two MODTRAN atmosphere models were used: Mid-Latitude Summer (294 K atmospheric temperature below 1 km altitude) and Sub-Arctic Winter (257 K atmospheric temperature below 1 km altitude), both with a Rural 23 km visibility aerosol model [7]. However, the default relative humidity (RH) parameter of the models was overridden and stepped from 10, 20, 30, 90% in order to determine the importance of atmospheric water vapour relative to optimum detector cut-off wavelengths.

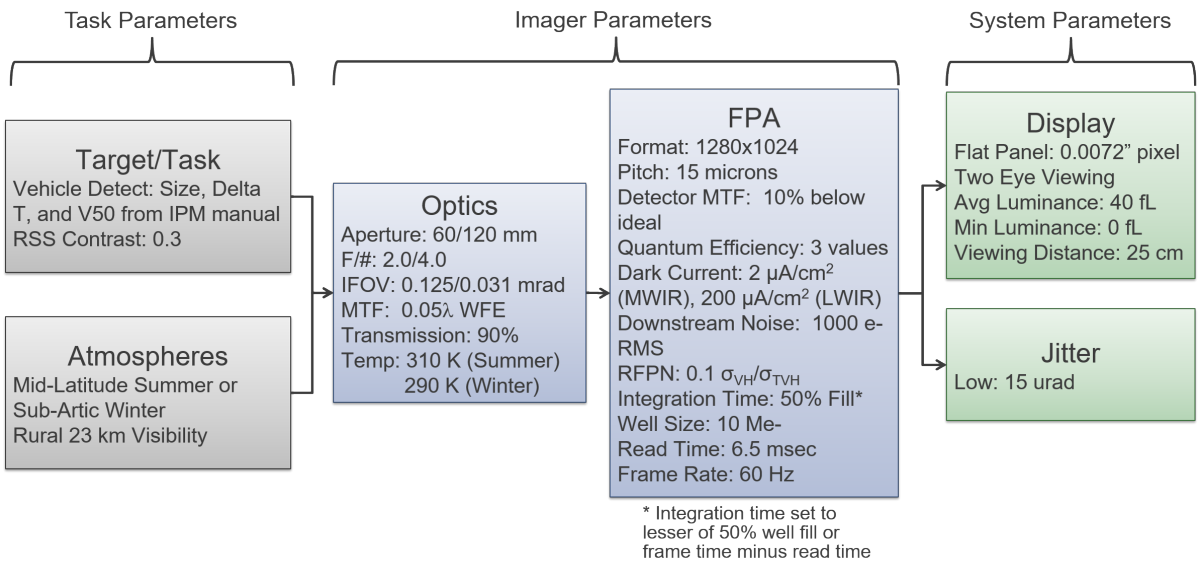

Fig. 5. Combinations of parameter values used in this analysis.

5. Modelling results

The objective of the IR system design trade space analysis described in the previous section was to determine the optimum detector spectral response, as defined by cut-on and cut-off wavelengths, for a variety of system designs, operational scenarios, and performance metrics. The dimensionality of the trade space precludes simple visualization of the results ensemble difficult, so trade-off trends were identified by filtering the results down to a single atmosphere, a single infrared band, and a single detector in-band QE value. Then the optimum detector spectral response bands for that combination of trade space values can be visualized as a function of RH. An example visualization is provided in Fig. 6, where the primary vertical axes of both charts are used to reference the optimum detector spectral bands which are represented as shaded regions as determined by either minimum at-aperture or at-range NETDs (blue regions) or maximum target detection range (green region). The secondary axis is used to reference the target detection ranges (normalized by the maximum range achieved for a given combination of sensor and atmospheric models) as a function of relative humidity that is achieved with the optimum detector spectral response as determined by either the minimum at-aperture NETD (solid line) or maximum target detection range (dashed line).

The results in Fig. 6 represent the specific case of the Mid-Latitude Summer atmosphere model, LWIR sensor model with F/2.0 optic, and 50% in-band detector QE. There are several performance trends observable in this case that were common in visualizations of the results for other cases in the trade space. First, the optimum detector response band as determined by the end-user performance metric (either detection or identification range) is narrower in width compared to the optimum band as determined by the system-level performance metric (NETD). Second, the centroid of the optimum detector band as determined by the end-user metric shifts to longer wavelengths with respect to increasing RH. Third, the optimum band as determined by the at-range NETD metric tends to become narrower as RH increases. Finally, the most important trend identified was that the end-user performance (target detection range) obtained with a detector response band optimized for the system-level NETD performance metric (either at-aperture or at-range) is always less (regardless of RH) than the performance obtained when the response band is optimized for end-user performance.

The results for the MWIR band were consistent with the trends identified for the LWIR band with some additional aspects as shown in the example provided in Fig. 7, which represent the specific case of the MWIR sensor model with F/4.0 optic and 50% in-band detector QE. The chart on the top plots results for the Mid-Latitude Summer atmosphere

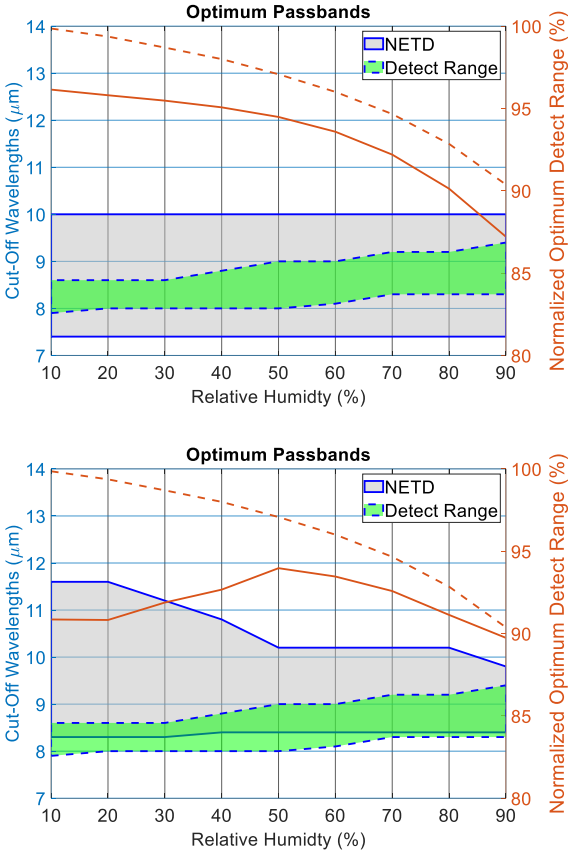

Fig. 6. Visualization of optimum detector spectral response bands (primary axes) with respect to either at-aperture NETD (top) or at-range NETD (bottom) and target detection range (both) and achieved target detection range (secondary axis) as a function of RH for the Mid-Latitude Summer atmosphere model, LWIR sensor model with F/2.0 optic, and 50% in-band detector QE.

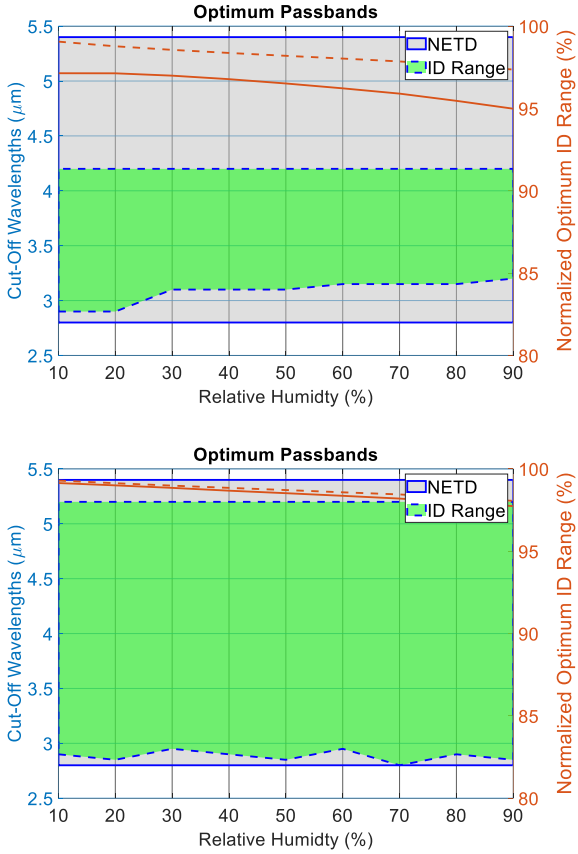

Fig. 7. Visualization of optimum detector spectral response bands (primary axes) with respect to at-aperture NETD and target identification range and achieved target identification range (secondary axis) as a function of RH for the Mid-Latitude Summer (top) or Sub-Arctic Winter (bottom) atmosphere models, MWIR sensor model with F/4.0 optic, and 50% QE.

model and shows that optimum response band for maximum end-user performance (target identification range) does not include wavelengths greater than the 4.3 μm CO_2 absorption notch whereas the optimum response band for minimum NETD performance does. This trend was observed to be consistent for cases where the detector integration time was sufficient to reach the desired 50% well fill criteria used for all the modelled cases. For cases when there was not sufficient flux to reach the desired well fill within the maximum allowable integration time, such as the case plotted in the bottom chart of Fig. 7 for the colder Sub-Arctic Winter environment, the optimum response band widened to include the longer wavelengths on the other side of the CO_2 notch. For these low flux cases (cold environment, larger F/#, and/or lower QE), the differences between the optimum detector response bands for the system-level and end-user performance were much smaller compared to those for the LWIR sensor models.

6. Conclusions

Before stating the authors' conclusions, some caveats to the analyses described in the previous sections should be stated. First, the "canned" MODTRAN atmosphere models used in the analyses may not adequately sample the ensemble of likely atmospheric conditions that an end-user may encounter. Furthermore, the presence of aerosols or obscurants with strong spectral features which may affect results were not considered.

With respect to the sensor models, flat QE spectral responses were assumed to identify trends, but the spectral shape of real-world detector response will influence optimum cut-off selection. Also, the NV-IPM sensor model automatically calculates the optical diffraction modulation transfer functions (MTFs) of the optics for each spectral response band iteration, but other performance-impacting relationships between optical design complexity and response band width were not considered in this analysis.

With respect to the modelled end-user scenarios, only ground-to-ground sensing tasks were considered. Results will vary for other scenarios, such as ground-to-air, space-to-ground, or spectrometry applications and scenarios.

With the above caveats taken into account, there are still some universal conclusions that the infrared system development community can obtain from the results. Most importantly, using lab-based system-level performance metrics to optimize system design for range-dependent end-user performance may not lead to maximum performance. In particular, system level designs should consider specifying response band maximum widths as opposed to minimum widths when specifying performance that FPA components need to achieve.

With respect to FPA designs, improving in-band or peak QE was observed to be more important than widening spectral response of detectors to maximum range-dependent performance. The use of a cold filter with a narrower passband to better match the optimum band may also offer other performance-enhancing avenues such as improving the FPA response spatial uniformity and/or the optical MTF of the lens system for even greater end-user performance.

References

[1] Rogalski, A. HgCdTe infrared detector material: history, status and outlook. *Rep. Prog. Phys.* **68** 2267 (2005) https://doi.org/10.1088/0034-4885/68/10/R01

[2] Dhar, N. K., Dat, R. & Sood, A. K. Advances in Infrared Detector Array Technology. in *Optoelectronics. Advanced Materials and Devices* (Eds. Pyshkin, S. L. & Ballato, J. M.) Ch. 7 (2013). https://doi.org/10.5772/5665

[3] Rogalski, A., Martyniuk, P. & Kopytko, M. Challenges of small-pixel infrared detectors: a review. *Rep. Prog. Phys*. **79**, 046501 (2016). https://doi.org/10.1088/0034-4885/79/4/046501

[4] Haran, T. L., James, J. Ch. & Cincotta, T. E. Relative performance analysis of IR FPA technologies from the perspective of system level performance. *Infrared Phys. Technol*. **84**, 7–20 (2017). https://doi.org/10.1016/j.infrared.2017.03.007

[5] Haran, T. L., James, J. Ch., Lane, S. E. & Cincotta, T. E. Quantum efficiency and spatial noise tradeoffs for III-V focal plane arrays. *Infrared Phys. Technol.* **97**, 309–318 (2019). https://doi.org/10.1016/j.infrared.2019.01.001

[6] U.S. Army CERDEC, Fort Belvoir, VA. Vollmerhausen, R. & Jacobs, E. *The targeting task performance (TTP) metric: a new model for predicting target acquisition performance.* Technical report AMSEL-NV-TR-230, 18–42, 47–51 (2006).

[7] Phillips Laboratory, Hanscon, Massachusetts. Kneizis, F. X. *et al. The Modtran 2/3. Report And Lowtran 7 Model* (1996).

[8] Asici, B. *et al*. The status of LWIR MCT detector development at ASELSAN. *Proc. SPIE* **11002**, 110021A (2019). https://doi.org/10.1117/12.2518867

[9] Cabrera, M. S. *et al*. Development of 13-μm cutoff HgCdTe detector arrays for astronomy. *Proc. SPIE* **5**, 036005 (2019). https://doi.org/10.1117/1.JATIS.5.3.036005

[10] Choi, K. K. *et al*. Long wavelength resonator-QWIP. *Proc. SPIE* **9819**, 981917 (2016). https://doi.org/10.1117/12.2224313

[11] Choi, K.K., Sun, S, & Olver, K. Resonator-QWIP FPA development. *Proc. SPIE* **9451**, 94512K (2015). https://doi.org/10.1117/12.2176446

[12] Choi, K. K. *et al*. Small pitch resonator-QWIP detectors and arrays. *Infrared Phys. Technol*. **94**, 118–125 (2018). https://doi.org/10.1016/j.infrared.2018.09.006

[13] Eich, D. *et al*. MCT-based high performance bispectral detectors by AIM. *J. Electron. Mater*. **48**, 6074–6083 (2019). https://doi.org/10.1007/s11664-019-07177-8

[14] Fastenau, J. M. *et al*. Direct MBE growth of metamorphic nBn infrared photodetectors on 150 mm Ge-Si substrates for heterogeneous integration. *J. Vac. Sci. Technol. B* **37**, 031216 (2019). https://doi.org/10.1116/1.5088784

[15] Huang, E. *et al*. Small pixel MWIR sensors for low SWaP applications. *Proc. SPIE* **11741**, 117410S (2021). https://doi.org/10.1117/12.2588774

[16] Huang, M. *et al*. InAs/GaAsSb type-II superlattice LWIR focal plane array detectors grown on InAs substrates. *IEEE Photon. Technol. Lett*. **32**, 453–456 (2020). https://doi.org/10.1109/LPT.2020.2973204

[17] Klipstein, P. C. *et al*. Development and production of array barrier detectors at SCD. *J. Electron. Mater*. **46**, 5386–5393 (2017). https://doi.org/10.1007/s11664-017-5590-x

[18] Klipstein, P. C. *et al*. Type II superlattice infrared detector technology at SCD. *J. Electron. Mater.* **47**, 5725–5729 (2018). https://doi.org/10.1007/s11664-018-6527-8

[19] Rubaldo, L. *et al*. Latest improvements on long wave p on n HgCdTe technology at Sofradir. *Proc. SPIE* **10177**, 101771E (2015). https://doi.org/10.1117/12.2264606

[20] Rubaldo, L. *et al*. Recent advances in Sofradir IR on II-VI photodetectors for HOT applications. *Proc. SPIE* **9755**, 97551X (2016). https://doi.org/10.1117/12.2208419

[21] Rubaldo, L. *et al*. State of the art HOT performances for Sofradir II-VI extrinsic technologies. *Proc. SPIE* **9819**, 98191l (2016). https://doi.org/10.1117/12.2229308

[22] Shkedy, L. *et al*. Development of 10μm pitch XBn detector for low SWaP MWIR applications. *Proc. SPIE* **9819**, 98191D (2016). https://doi.org/10.1117/12.2220395

[23] Shkedy, L. *et al*. HOT MWIR detector with 5 um pitch. *Proc. SPIE* **11741**, 117410W (2021). https://doi.org/10.1117/12.2585374

[24] Sun, J. *et al*. Advanced inductively coupled plasma etching processes for fabrication of resonator-quantum well infrared photodetector, *Infrared Phys. Technol*. **70** 25–29 (2015). https://doi.org/10.1016/j.infrared.2014.09.022

[25] Sun, J. N. & Choi, K. K. Fabrication of resonator-quantum well infrared photodetector focal plane array by inductively coupled plasma etching. *Proc. SPIE* **55**, 026119 (2016). https://doi.org/10.1117/1.OE.55.2.026119

[26] Sun, J., Choi, K. K., Olver, K. & Fu, R. X. Fabrication of resonator-quantum well infrared photodetector (R-QWIP) with 10.2 µm cutoff. *Proc. SPIE* **9609**, 96090J (2015). https://doi.org/10.1117/12.2186433

[27] Ting, D. Z. *et al*. InAs/InAsSb type-II superlattice mid-wavelength infrared focal plane array with significantly higher operating temperature than InSb. *IEEE Photon. J*. **10**, 1–6 (2018). https://doi.org/10.1109/JPHOT.2018.2877632

[28] Choi, K. K., Allen, S. C., Sun, J. G. & DeCuir, E. A. Resonant detectors and focal plane arrays for infrared detection. *Infrared Phys. Technol*. **84**, 94–101 (2017). https://doi.org/10.1016/j.infrared.2016.12.005

[29] Deng, G., Yang, W., Peng, Z. & Zhang, Y. High operating temperature InAsSb-based mid-infrared focal plane array with a band-aligned compound barrier. *Appl. Phys. Lett*. **116**, 031104 (2020). https://doi.org/10.1063/1.5133093

[30] Gunapala, G. *et al*. Antimonides T2SL mid-wave and long-wave infrared focal plane arrays for earth remote sensing applications. *Proc. SPIE* **11288**, 112880K (2020). https://doi.org/10.1117/12.2543896

[31] Höglund, L. *et al*. Type-II superlattice SWaP IDDCA production at IRnova. *Proc. SPIE* **11407**, 114070P (2020). https://doi.org/10.1117/12.2558707

[32] Ivanov, R. *et al*. III-V based infrared detectors are imposing new standards. *Proc. SPIE* **11407**, 114070Q (2020). https://doi.org/10.1117/12.2558736

[33] Jiang, Zh. *et al*. Mid/-long-wave dual-band infrared focal plane array based on type-II InAs/GaSb superlattice. *Proc. SPIE* **10826**, 108261X (2018). https://doi.org/10.1117/12.2506053

[34] Kimura, D. *et al*. Quantum well infrared imaging sensor with high-sensitivity in the wavelength range of up to 15 µm. *SEI Techn. Rev*. **86**, 41–44 (2018). https://sumitomoelectric.com/sites/default/files/2020-12/download_documents/86-08.pdf

[35] Klipstein, P. C. *et al*. HOT MWIR technology at SCD. *Proc. SPIE* **12107**, 121070Q (2022). https://doi.org/10.1117/12.2615622

[36] Klipstein, P. C. *et al*. Low SWaP MWIR detector based on XBn focal plane array. *Proc. SPIE* **8704**, 87041S (2013). https://doi.org/10.1117/12.2015747

[37] Oguz, F. *et al*. High performance 15-µm pitch 640×512 MWIR InAs/GaSb type-II superlattice sensors. *IEEE J. Quantum Electron*. **58**, 1–6 (2022). https://doi.org/10.1109/JQE.2021.3129535

[38] Rafol, B. *et al*. Modulation transfer function measurements of type-II mid- wavelength and long-wavelength infrared superlattice focal plane arrays *Infrared Phys. Technol*. **96**, 251–261 (2019). https://doi.org/10.1016/j.infrared.2018.11.006

[39] Soibel, A. *et al*. Mid-wavelength infrared InAsSb/InAs nBn detectors and FPAs with very low dark current density. *Appl. Phys .Lett.* **114**, 161103 (2019). https://doi.org/10.1063/1.5092342

[40] Sun, J., Choi, K. K, Olver, K. A. & Fu, R. X. Design and fabrication of resonator-QWIP for SF_6 gas sensor application. *Proc. SPIE* **10149**, 101490S (2017). https://doi.org/1117/12.2257990

[41] Teng, T. *et al.* Demonstration of MOCVD-grown long-wavelength infrared InAs/GaSb superlattice focal plane array. *IEEE Access* **9**, 60689–60694 (2021). https://doi.org/10.1109/ACCESS.2021.3072845

[42] Ting, D. Z. *et al*. Antimonide e-SWIR, MWIR, and LWIR barrier infrared detector and focal plane array development. *Proc. SPIE* **10624**, 1062410 (2018). https://doi.org/10.1117/12.2305248

[43] Ting, D. Z. *et al*. Long wavelength InAs/InAsSb superlattice barrier infrared detectors with p-type absorber quantum efficiency enhancement. *Appl. Phys. Lett*. **118**, 133503 (2021). https://doi.org/10.1063/5.0047937

[44] Wang, L. *et al*. Fabrication and characterization of InAs/GaSb type-II superlattice long-wavelength infrared detectors aiming high temperature sensitivity. *J. Light. Technol*. **38**, 6129–6134 (2020). https://doi.org/10.1109/JLT.2020.3005974

[45] Cervera, C. *et al*. Low-dark current p-on-n MCT detector in long and very-long wavelength infrared. *Proc. SPIE* **9451**, 945129 (2015). https://doi.org/10.1117/12.2179216

[46] Hanna, S. *et al*. Low dark current LWIR and VLWIR HgCdTe focal plane arrays at AIM. *Proc. SPIE* **10000**, 100000P (2016). https://doi.org/10.1117/12.2244514

[47] Lee, D. *et al*. Law 19: The ultimate photodiode performance metric. *Proc. SPIE* **11407**, 114070X (2020) . https://doi.org/10.1117/12.2564902

[48] Baier, N. *et al*. MCT planar p-on-n LW and VLW IRFPAs. *Proc. SPIE* **8704**, 87042P (2013). https://doi.org/10.1117/12.2016369

[49] Eich, D. *et al*. Progress of MCT detector technology at AIM towards smaller pitch and lower dark current. *J. Electron. Mater*. **46**, 5448–5457 (2017). https://doi.org/10.1007/s11664-017-5596-4

[50] Hanna, S. *et al*. MCT-Based LWIR and VLWIR 2D focal plane detector arrays for low dark current applications at AIM. *J. Electron. Mater*. **45**, 4542–4551 (2016). https://doi.org/10.1007/s11664-016-4523-4

[51] Péré-Laperne, N. *et al*. Improvements of long wave p on n HgCdTe infrared technology. *Proc. SPIE* **9933**, 99220H (2016). https://doi.org/10.1117/12.2241440

[52] Craig, A. P., Letka, V., Carmichael, M., Golding, T. & Marshall, A. R. InAsSb-based detectors on GaSb for near-room-temperature operation in the mid-wave infrared. *Appl. Phys. Lett*. **118**, 251103 (2021). https://doi.org/10.1063/5.0051049

[53] Deng, G. *et al*. High operating temperature pBn barrier mid-wavelength infrared photodetectors and focal plane array based on InAs/InAsSb strained layer superlattices. *Opt. Express* **28**, 17611–17619 (2020). https://doi.org/10.1364/OE.395770

[54] Gunapala, S. *et al.* Long-Wavelength Infrared Digital Focal Plane Arrays For Earth Remote Sensing Applications. in *IGARSS 2019 IEEE International Geoscience and Remote Sensing Symposium* 8856–8859 (2019). https://doi.org/10.1109/IGARSS.2019.8900531

[55] Huang, M. *et al*. InAs/GaAsSb type-II superlattice LWIR focal plane arrays detectors grown on InAs substrates. *IEEE Photon. Technol. Lett.* **32**, 453–456 (2020). https://doi.org/10.1109/LPT.2020.2973204

[56] Jiang, Z. *et al*. Mid-/long-wave dual-band infrared focal plane array based on type-II InAs/GaSb superlattice. *Proc. SPIE* **10836**, 108261X (2018). https://doi.org/10.1117/12.2506053

[57] Kaya, Y. *et al*. Two-band ZnCdSe/ZnCdMgSe quantum well infrared photodetector. *AIP Adv*. **8**, 075105 (2018). https://doi.org/10.1063/1.5013607

[58] Kopytko, M. *et al*. Investigation of surface leakage current in MWIR HgCdTe and InAsSb barrier detectors. *Semicond. Scie. Technol*. **33**, 125010 (2018). https://doi.org/10.1088/1361-6641/aae768

[59] Lee, H. J. *et al*. Dark current improvement due to dry-etch process in InAs/GaSb type-II superlattice LWIR photodetector with nBn structure. *Infrared Phys. Technol.* **94**, 161–164 (2018). https://doi.org/10.1016/j.infrared.2018.09.009

[60] Lee, H. J., Ko, S. Y., Kim, Y. H. & Nah, J. Surface leakage current reduction of InAsSb nBn MWIR HOT detector via hydrogen peroxide treatment. *Infrared Phys. Technol.* **112**, 103597 (2021). https://doi.org/10.1016/j.infrared.2020.103597

[61] Martijn, H. *et al*. QWIPs at IRnova, a status update. *Proc. SPIE* **9819**, 981918 (2016). https://doi.org/10.1117/12.2228348

[62] Péré-Laperne, N. *et al*. Latest developments of 10 µm pitch HgCdTe diode array from the legacy to the extrinsic technology. *Proc. SPIE* **9819**, 981920 (2016). https://doi.org/10.1117/12.2228720

[63] Ting, D. Z. *et al*. Mid-wavelength high operating temperature barrier infrared detector and focal plane array. *Appl. Phys. Lett*. **113**, 021101 (2018). https://doi.org/10.1063/1.5033338

[64] Ting, D. Z. *et al*. Type-II superlattice mid-wavelength infrared focal plane arrays for CubeSat hyperspectral imaging. *IEEE Photon. Technol. Lett.* **34**, 329–332 (2022). https://doi.org/10.1109/LPT.2022.3156048

[65] Wang, F. *et al*. Fabrication of a 1024×1024 format long wavelength infrared focal plane array based on type-II superlattice and barrier enhanced structure. *Infrared Phys. Technol*. **115**, 103700 (2021). https://doi.org/10.1016/j.infrared.2021.103700

[66] Wang, L. *et al*. Investigation of low frequency noise-current correlation for the InAs/GaSb T2SL long-wavelength infrared detector. *Opt. Quantum Electron*. **54**, 286 (2021). https://doi.org/10.1007/s11082-021-03450-5

[67] Xu, J. *et al*. Effects of etching processes on surface dark current of long-wave infrared InAs/GaSb superlattice detectors. *Infrared Phys. Technol.* **107**, 103277 (2020). https://doi.org/10.1016/j.infrared.2020.103277

[68] Diel, W. *et al*. High-resolution QWIP and T2SL IDDCAs by IRnova. *Proc. SPIE* **10624**, 1062410 (2018). https://doi.org/10.1117/12.2304865

[69] Höglund, L. *et al*. Advantages of T2SL: results from production and new development at IRnova. *Proc. SPIE* **9819**, 98180Z (2016). https://doi.org/10.1117/12.2227466

[70] Klipstein, P. C. *et al*. Type II superlattice technology for LWIR detectors. *Proc. SPIE* **9819**, 98190T (2016). https://doi.org/10.1117/12.2222776

[71] Nghiem, J. *et al*. Radiometric characterization of type II InAs/GaSb superlattice (T2SL) midwave infrared photodetectors and focal plane arrays. *Proc. SPIE* **10562**, 105623Y (2016). https://doi.org/10.1117/12.2296053

[72] Rubaldo, L. *et al*. Achievement of high image quality MCT sensors with Sofradir vertical industrial model. *Proc. SPIE* **10624**, 106240U (2018). https://doi.org/10.1117/12.2307344

[73] Ribet-Mohamed, I. *et al*. Temporal stability and correctability of a MWIR T2SL focal plane array. *Infrared Phys. Technol*. **96**, 145–150 (2019). https://doi.org/10.1016/j.infrared.2018.10.028

[74] Rubaldo, L. *et al*. Image quality improvement against the backdrop of SWAP and pitch reduction. *Proc. SPIE* **11002**, 1100219 (2019). https://doi.org/10.1117/12.2520412

[75] Ivanov, R. *et al*. QWIP as solution for mobile VLWIR imaging systems. *Proc. SPIE* **11741**, 117411F (2021). https://doi.org/10.1117/12.2588556

[76] Tennant, W. R. "Rule 07" revisited: Still a good heuristic predictor of p/n HgCdTe photodiode performance? *J. Electron. Mater*. **39**, 1030–1035 (2010). https://doi.org/10.1007/s11664-010-1084-9

[77] Rogalski, A. Quantum well photoconductors in infrared detector technology. *J. Appl. Phys*. **93**, 4355–4391 (2003). https://doi.org/10.1063/1.1558224

[78] Rhiger, D. R. Performance comparison of long-wavelength infrared type II superlattice devices with HgCdTe. *J. Electron. Mater*. **40**, 1815–18225 (2011). https://doi.org/10.1007/s11664-011-1653-6